Use of optical techniques to evaluate the ionizing radiation effects on biological specimens

Hideaki Fujita[1] and Tomonobu M. Watanabe[1,2,*]

[1]Department of Stem Cell Biology, Research Institute for Radiation Biology and Medicine, Hiroshima University, Minami-ku, Hiroshima 734-0037, Japan
[2]Laboratory for Comprehensive Bioimaging, RIKEN Center for Biosystems Dynamics Research (BDR), Chuo-ku, Kobe 650-0047, Japan

*Corresponding author. Laboratory for Comprehensive Bioimaging, RIKEN Center for Biosystems Dynamics Research (BDR), Chuo-ku, Kobe 650-0047, Japan.
Tel: +8182-257-5938 or +81-78-306-3425; Email: tomowatanabe@riken.jp or twatanabe@hiroshima-u.ac.jp

ABSTRACT

Radiation induces various changes in biological specimens; however, the evaluation of these changes is usually complicated and can be achieved only through investment in time and labor. Optical methods reduce the cost of such evaluations as they require less pretreatment of the sample, are adaptable to high-throughput screening and are easy to automate. Optical methods are also advantageous, owing to their real-time and onsite evaluation capabilities. Here, we discuss three optical technologies to evaluate the effects of radiation on biological samples: single-molecule tracking microscopy to evaluate the changes in the physical properties of DNA, Raman spectral microscopy for dosimetry using human hair and second-harmonic generation microscopy to evaluate the effect of radiation on the differentiation of stem cells. These technologies can also be combined for more detailed information and are applicable to other biological samples. Although optical methods are not commonly used to evaluate the effects of radiation, advances in this technology may facilitate the easy and rapid assessment of radiation effects on biological samples.

Keywords: Raman; SHG; single-molecule; imaging; microscopy; radiation

INTRODUCTION

Assessment of the effects of radiation, both ionizing and non-ionizing, on biological specimens, such as cells or tissues, is of primary interest in the field of radiation biology. Exposure to radiation can occur under various circumstances. Environmental radiation can be caused by long-lived radioactive atoms in the soil, air or building materials or by high-energy particles from space [1–3]. Exposure to cosmic rays can occur during long flights [4]. Medical radiation exposure occurs during diagnostic procedures, such as X-ray imaging, computed tomography scans or mammography, or during therapeutic procedures for the treatment of cancer [5–7]. A nuclear plant disaster can affect many people. In the Chernobyl disaster that occurred on 26 April 1986, ~350 000 people were exposed to radiation in the thyroid gland [8]. The tragic accidents at Chernobyl and Fukushima have resulted in the radioactive pollution of soil and water in a wide area [9], affecting the living organisms. In an event of nuclear disaster, both external and internal radiation exposure with various types of radiation having different dose rates may occur, which will alter the effects on living organisms. Therefore, effects of radiation exposure should be studied from various angles

using different measurement modalities, as various causes may affect biological specimens differently.

In the long history of radiation biology, various methods have been developed to evaluate the effects of radiation on biological specimens. In general, biochemical methods, such as expression profiling of related genes involved in stress response or DNA repair and γH2AX assay, which visualizes the DNA repair foci, are often used, which focus on the effect of radiation to biological activities. Although radiation affects various cell constituents, such as proteins, lipids and carbohydrates, its largest impact is the damage caused to the DNA. Thus, methods to detect DNA damage, such as the G-band assay, which examine banding patterns of chromosomes with Giemsa staining [10], and the comet assay, which visualizes DNA damage in single cells by electrophoresis [11], are considered to be standard assay procedures. The dicentric chromosome assay is an internationally recognized method for assessing the ionizing radiation dose to which an individual is exposed [12]. Since dicentric chromosomes are rare in nature, the amount of ionizing radiation experienced by an individual can be estimated by counting abnormal dicentric chromosomes in cells.

Although these methods are well established and can detect the effects of radiation, the procedure is time-consuming and requires a trained operator.

Since biological reactions to radiation exposure depend on the dose, the exposure dose can be retrospectively estimated from the degree of the reaction. However, the quantitative nature of this method for dosimetry is low, owing to individual and/or organ differences [13–15]. Measuring the radiation of the environment can be performed more quantitatively and rapidly compared to measuring that of biological activities, as pretreatment of samples is not required. Neutron activation occurs when neutrons collide with atomic nuclei and are absorbed, creating heavier radioactive isotopes that decay with the radiation. In human body, one of the most important atoms in neutron activation is ^{23}Na, where with neutron activation turns to ^{24}Na which emits γ-ray with the half-life of 14.96 h when decaying to ^{24}Mg. By measuring this γ-ray, neutron dose of the individual exposed can be estimated. Bone and tooth enamel samples are often used in retrospective dosimetry [16, 17]. The most typical modality in dosimetry for monitoring the effect on a specimen is magnetic, which provides electron paramagnetic resonance (EPR) or electron spin resonance (ESR), which detects unpaired electrons in paramagnetic materials. Hence, the unpaired electrons generated by ionizing radiation on the nail or tooth enamel were measured using EPR/ESR dosimetry [18, 19]. Optically stimulated luminescence (OSL) or thermally stimulated luminescence (TSL) is a phenomenon in which electrons trapped within the crystal lattice defects, as crystalline materials absorb ionizing radiation, emit photons when excited by light or heat. Human α-keratin contained in nail or hair cause OSL/TSL, which can be used for dosimetry [20]. Although EPR/ESR dosimetry has many advantages, it is a complicated and expensive process.

Light or optics, which are the oldest modalities used in the biomedical field, provide large quantities of data, high voxel resolution and simple and rapid testing methods. Fluorescence microscopy enables the quantification of biological dysfunction in living cells and tissues induced by radiation exposure [21, 22]. Scattering light, such as Raman scattering, provides not only information related to metabolic reactions but also chemical information on molecular bonds [23, 24], which can be reorganized by radiation irradiation directly or through production of reactive oxygen species (ROS) [25, 26]. Optical modalities have not reached the mainstream because of their low sensitivity when used in scattering spectroscopy. Nowadays, the manufacturing technology for optical elements, such as lenses and mirrors, has advanced, and the sensitivity of photodetector elements has significantly improved. Moreover, improvements in computer performance have enabled to handle vast amounts of microscopic image data, and different types of biological information can be extracted from these data [27, 28]. In this brief review, we discuss various optical techniques to evaluate the effects of radiation on biological specimens: single-molecule tracking detects changes in the dynamics of transcription factors that reflect the physical properties of DNA, Raman spectroscopy for dosimetry using human white hair and second-harmonic generation (SHG) microscopy to evaluate long-term effects on cardiomyogenesis. We hope that this review will facilitate to develop a novel optical method for the easy evaluation of radiation effects on biological specimens.

OPTICAL METHODS FOR THE EVALUATION OF THE EFFECTS OF RADIATION
Single-molecule microscopy

The greatest advantage of fluorescent microscopy is its applicability to monitor the dynamic behaviors of the proteins of interest in a living cell or tissue by conjugating a fluorescent dye to the protein, enabling fluorescent microscopy as the most common tool in general biology. In radiology, fluorescence microscopy is not only used as a standard observation tool but also as a fundamental technology for γH2AX and G-band assays.

The ultimate sensitivity in fluorescence microscopy is that of the 'single molecule' of protein. By ensuring that the fluorescent dyes are sparsely distributed and background fluorescence is low using a total internal reflection fluorescence microscope [29], a highly inclined laminated optical (HILO) sheet microscope [30], or similar techniques, single protein molecules can be visualized individually. Herein, we attempted to establish an easy method to simultaneously evaluate three types of effects of radiation in living cells: changes in the expression of a transcription factor, metabolic activity of a ROS scavenger and mechanical properties of the DNA strand using single-molecule microscopy.

In a previous study, mouse embryonic stem cells (mESCs) were the model sample, and Nanog, which is a transcription factor for pluripotency maintenance, was the target protein [31]. To simplify the experiment, ultraviolet (UV) irradiation was used instead of ionizing radiation. Cells were seeded on glass bottom dish and UV light of 340 nm at 2 mJ/mm^2 was irradiated to mESC, expressing green fluorescent protein-tagged Nanog (Nanog-GFP). Single molecules of Nanog-GFP were tracked immediately and 24 h after UV irradiation and were compared with those without UV irradiation using custom-built HILO microscope based on Nikon N-Storm (Nikon, Tokyo, Japan) equipped with charge-coupled device camera (iXon3 893, Andor Technology, Belfast, UK). Before single-molecule microscopy observation, an increase in ROS production and mitochondrial fragmentation induced by UV irradiation were confirmed with the commercialized fluorescence indicators CellROX staining (Fig. 1A) and MitoTracker (Fig. 1B), which was consistent with the previous results [32].

The change in the expression level of Nanog upon UV irradiation was easily observed by fluorescence intensity within the nucleus that; UV irradiation did not affect Nanog expression (Fig. 1C). By temporarily photobleaching GFP within the observation field of view, single molecules that newly entered the field can be individually visualized (Fig. 1D). The photobleaching rate depends on the ROS activity as photobleaching is an oxidation reaction of fluorophores by ROS, and ROS scavengers reduce photobleaching by ROS produced by laser illumination. Immediately after UV irradiation, the photobleaching rate increased, indicating a reduction in ROS scavenger activity. One day after UV irradiation, the decrease in fluorescence intensity by photobleaching was same as that of the cells without UV irradiation, indicating the recovery of ROS scavenger activity over time (Fig. 1E). Using the photobleached cells, single molecules of Nanog-GFP were tracked and the mean square displacement (MSD) [33, 34], which is the deviation of the position from a reference position, of each track was analyzed. Since the movement of proteins in a cell is
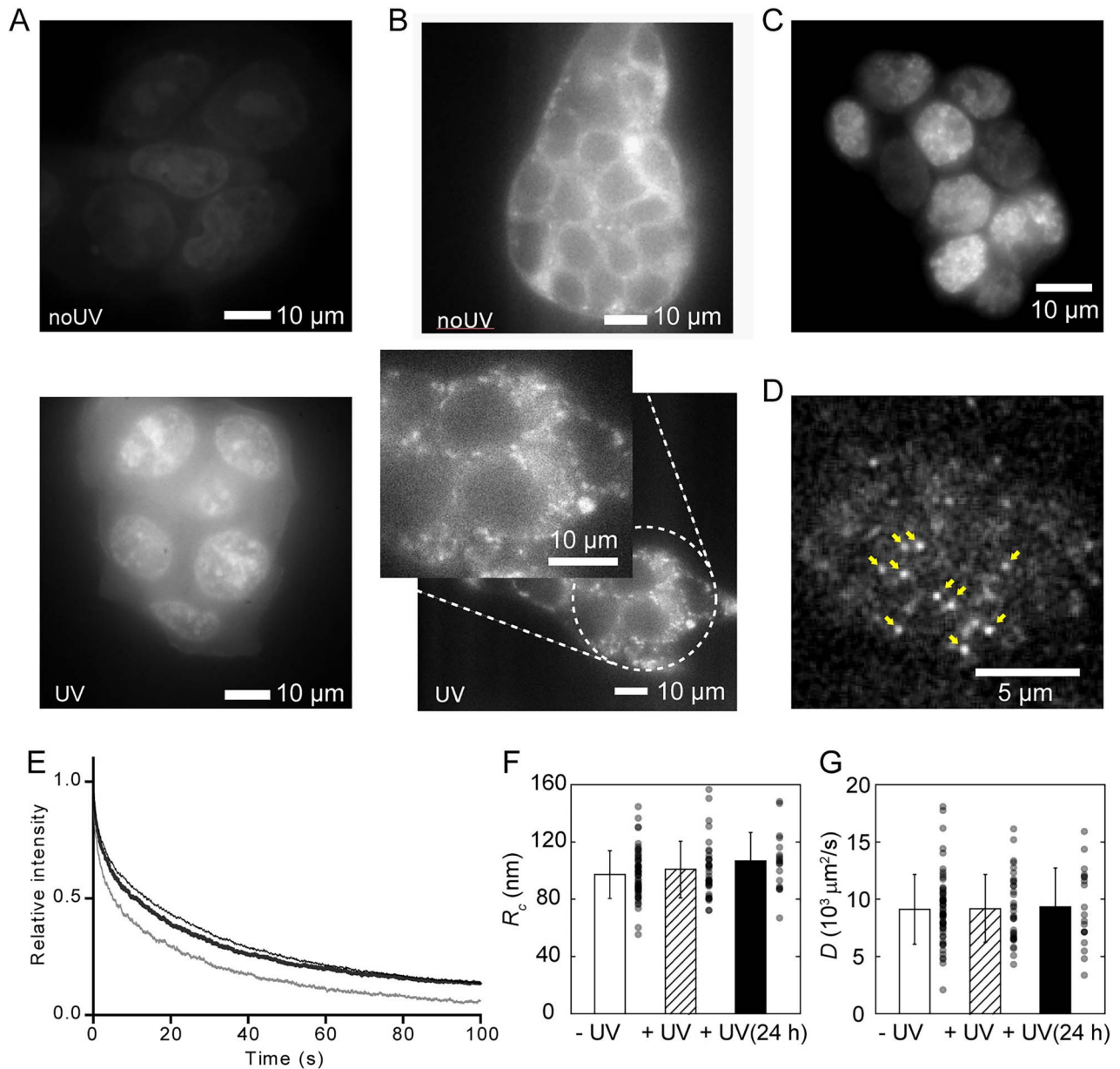
Fig. 1. Effects of UV radiation on mESCs. (A) Cells stained with CellROX without (above) or with (below) UV irradiation. **(B)** Cells stained with MitoTracker without (above) or with (below) UV irradiation. (Inset) Magnified image showing the fragmented mitochondria. **(C)** Fluorescent image of mouse ESCs expressing the Nanog-GFP after UV irradiation. **(D)** Single molecules of Nanog-GFP observed via HILO illumination. Typical single-molecule fluorescence spots are indicated by arrows. **(E)** Time-dependent change in fluorescent intensity during photobleaching before single molecule observation of Nanog-GFP-expressing mouse ESC nucleus without UV irradiation (hairline) just after UV irradiation (thin line) and 24 h after UV irradiation (thick line). **(F, G)** Confined radius (R_c) **(F)** and diffusion constant (D) **(G)** measured via single-molecule tracking without UV irradiation (open) just after UV irradiation (dashed) and 24 h after UV irradiation (filled). **Error bar represents the standard deviation (SD).** $n = 35$ for –UV, 56 for +UV and 19 for +UV (24 h). **Reproduced from Okamoto *et al.*, 2023 [31].**

dominated by diffusion based on Brownian motion and restricted by interactions with other elastic components, such as the cytoskeleton and DNA strands, the speed (diffusion constant, D) and range (confined radius, R_c) of diffusion are reflected in the MSD [33]. In our study, R_c increased slightly with UV irradiation, although the difference was not statistically significant (Fig. 1F), and D did not change after

UV irradiation (Fig. 1G). This result indicates that the chromatin opened slightly upon UV irradiation, which is consistent with previous findings [35, 36].

Using single-molecule microscopy, we successfully evaluated the effects of UV light on the functions of ROS scavengers and changes in the physical properties of DNA. The results of single-molecule microscopy revealed that with UV irradiation, ROS scavenger function decreased, possibly due to the degradation of antioxidants triggered by mitochondrial damage, which recovered after 24 h. Although UV irradiation only negligibly affects the diffusion movement of Nanog, it may significantly affect other transcription factors and proteins.

Raman spectral microscopy for hair dosimetry

In radiation accidents or disasters, the radiation dose experienced by an individual should be estimated as it can be used as a reference to determine the treatment plan for the individual or for epidemiological studies. For retrospective dosimetry, bone or tooth enamel samples from individuals are often collected for EPR/ESR or OSL/TSL measurements as signals are more stable compared to cell-based methods, such as γH2AX or dicentric chromosome assay [37–39]. These methods are well established and can measure doses from $\sim$100 mSv and above; however, sample collection is often difficult and invasive methods, such as bone biopsy, are needed. To overcome the difficulty of sample collection, nails and hair have attracted attention, owing to their low invasiveness in sample collection. Both nails and hair are mainly composed of fibrillar protein keratin, and they have been proved useful for retrospective radiation dosimetry [20, 40, 41]. In addition to the aforementioned methods, Raman spectroscopy can be used for dosimetry. Raman spectra of the samples reflect the state and abundance of chemical bonds within the material; thus, they may detect structural alterations and induced defects in the crystal lattice caused by ionizing radiation. A recent report showed that Raman spectroscopy can distinguish between non-irradiated and X-ray-irradiated red blood cells [42].

To further assess the possibility of using Raman spectroscopy in radiation dosimetry, we evaluated whether γ-ray irradiation changes the Raman spectrum of human white hair. Human white hair was irradiated at 2, 5 and 20 Gy using a Gammacell-40 Exactor (MDS Nordion) at 12.5 mGy/s, and Raman spectra were measured using a home-built Raman microscope equipped with a 532 nm laser [43]. Irradiated and non-irradiated hair samples were attached between two coverslips with an adhesive tape where the gap between coverslips were immersed with water and edges were sealed with enamel (Fig. 2A). Raman spectra were obtained using $\times$40 water immersion objective lens (Nikon) with 5 min exposure. Obtained spectra was processed using home-built software using Microsoft Visual C++. Raman spectra was obtained from 14 (0 Gy), 18 (2 Gy), 17 (5 Gy) and 12 (20 Gy) hairs. Statistical analysis was performed using Microsoft Excel (Redmond, WA). Human white hair samples were purchased from Ketabaya (Tokyo, Japan). In comparison to Raman spectrum of non-irradiated white hair, a slight change was observed in the Raman spectra of white hair irradiated at 5 and 20 Gy in the fingerprint region (700–1800 cm^{-1}; Fig. 2B). Conversely, CH region (2600–3200 cm^{-1}) of the Raman spectra were almost identical between non-irradiated and γ-ray irradiated white hair (Fig. 2C). To visualize the change in Raman spectrum by γ-ray irradiation, difference spectra were calculated between non-irradiated

hair where the averaged 0 Gy spectrum was subtracted from 2 (green), 5 (orange) and 20 Gy (red) averaged spectra (Fig. 2D). The difference spectra showed that there were peaks that were largely changed by 5 and 20 Gy irradiation in the opposite direction to 2 Gy irradiation (Fig. 2D, arrows). Probably, these peaks could be used as markers for radiation. To confirm this, we calculated the peak ratio of 1334/1003 and 1628/2953 (Fig. 2E). These peaks were attributed to phenylalanine (1003 cm^{-1}), amide-III (1334 cm^{-1}), amide-I (1628 cm^{-1}) and CH$_3$ stretching (2958 cm^{-1}) [44, 45]. For the 1334/1003 value, there were no differences between non-irradiated and 2 Gy-irradiated hair; however, an increase was observed in 5 Gy- and 20 Gy-irradiated hair (Fig. 2E, left). For the 1628/2958 value, a slight decrease was observed in 2 Gy-irradiated hair, whereas an increase was observed in 5 Gy- and 20 Gy-irradiated hair compared to non-irradiated hair (Fig. 2E, right). This result indicates that these peaks can be used to identify hair irradiated at 5 Gy and above. To further examine the difference between Raman spectra from non-irradiated and γ-ray irradiated hair, we performed discriminant analysis of principal components (DAPC) to the fingerprint region of the Raman spectra (Fig. 2F). DAPC score plot showed that 0 and 2 Gy spectra were located in the same region, whereas 5 and 20 Gy spectra were located in a different location compared to 0 and 2 Gy spectra in the score plot (Fig. 2F).

These results show that Raman spectra from white hair can be used to distinguish between 0 and 2 Gy γ-ray irradiation and >5 Gy irradiation, however, it is not capable of distinguishing the dose <2 Gy. The peaks that showed major difference with γ-ray irradiation >5 Gy were mostly protein-related, which is reasonable because hair is mostly composed of proteins. Our finding is consistent with the previous report that revealed γ-ray irradiation caused changes in the Raman spectra of human black hair, although only the 1370 cm^{-1}/1589 cm^{-1} ratio of the first-order Raman spectra focusing on carbon structure was examined [46]. We believe that the further development of this method will enable the use of Raman spectroscopy in retrospective biodosimetry.

Assessment of the tardive effects of radiation on cardiomyocytes using SHG microscopy

The stochastic effects of radiation are mostly focused on oncogenesis or heritable diseases, as they are often prominent and have a significant influence on the individual. Besides these effects, surviving stem cells still possess pluripotency and can differentiate into functional cells [47, 48]. However, cells that are differentiated from radiation-damaged cells may possess abnormalities compared with normal cells. A recent report showed that cardiomyocytes differentiated from X-ray-irradiated ESC had beating abnormalities [48], indicating that the radiation exposure of stem cells may cause functional abnormalities in cardiomyocytes. Cardiomyocyte abnormalities can be assessed using various methods, such as the hERG or QT assay; however, these methods target ion channels [49, 50]. Since the primary function of cardiomyocytes is to generate force and contract, an assay to evaluate the force-generating capability of myosin motors is preferable. While heartbeat measurement based on video analysis and sarcomere length measurement is a simple, non-invasive method for evaluating cardiomyocyte dysfunction, it provides no information on the mechanism of force generation failure. We applied a method to estimate the actomyosin crossbridge
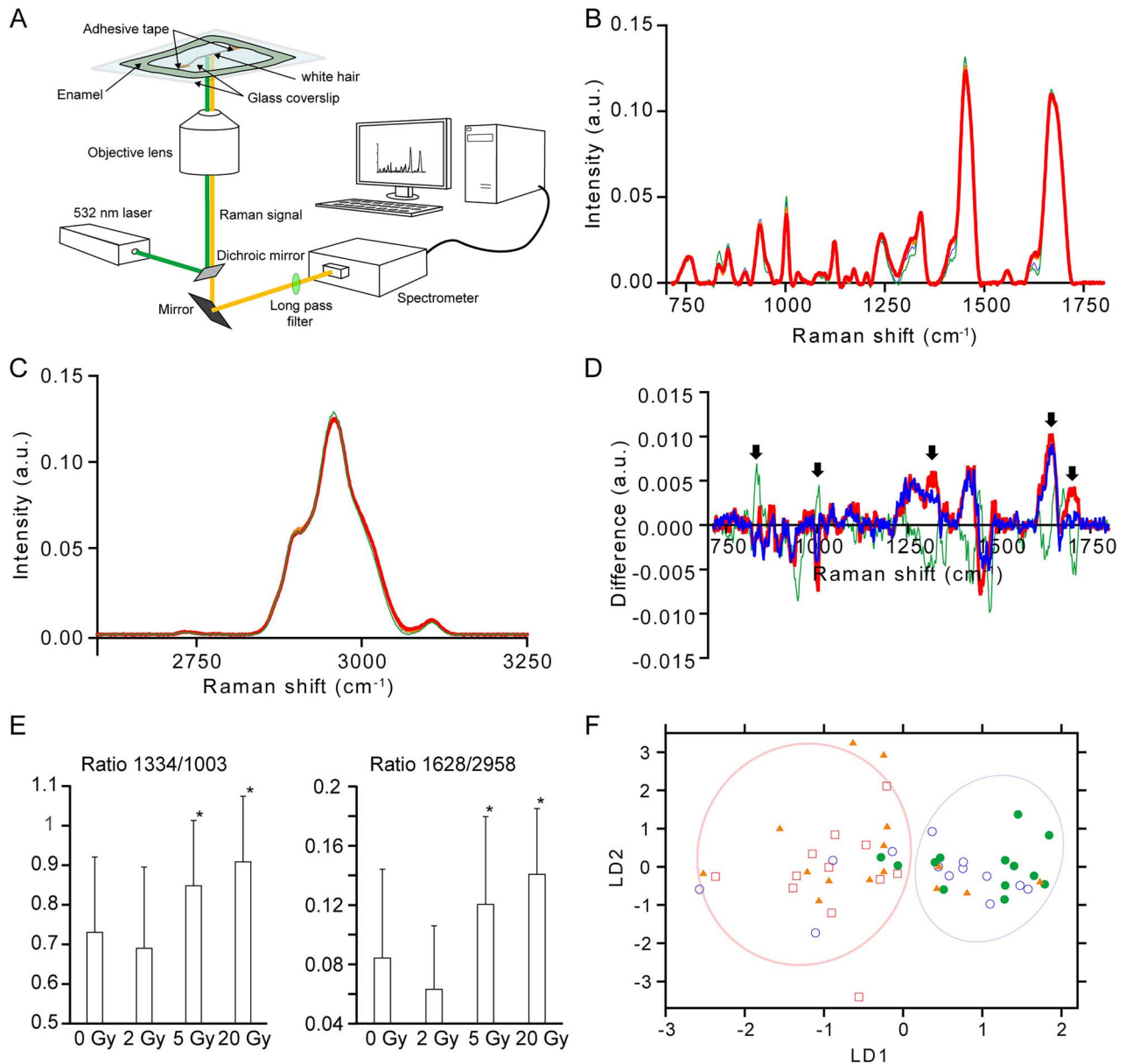
Fig. 2. Change in Raman spectra by γ-ray irradiation. (A) Schematic illustration of the experimental setup. **(B)** Averaged Raman spectra of human white hair without γ-ray irradiation (hairline) and with 2 Gy (thin line), 5 Gy (medium line) and 20 Gy (thick line) irradiation in the fingerprint region. **(C)** Averaged Raman spectra of human white hair in the CH region. Line indication is same as in **(B)**. **(D)** Differences in the Raman spectra of the fingerprint region. Raman spectrum of human white hair without γ-ray irradiation was subtracted from the 2 Gy (thin line), 5 Gy (medium line) and 20 Gy (thick line) Raman spectra. **(E)** Peak value ratio of human white hair Raman spectra with and without γ-ray irradiation. (Left) 1334/1003; (right) 1629/2958. Error bar represents the SD. Asterisks indicate the statistical significance ($P < 0.05$) at 0 Gy via the Student's t-test. **(F)** DAPC score plot of human white hair Raman spectrum in the fingerprint region. Each symbolshow hair with irradiation at 0 Gy (open circle), 2 Gy (filled circle), 5 Gy (filled triangles) and 20 Gy (open squares), 2 Gy (filled circle).

state in beating cardiomyocytes based on SHG microscopy to investigate the acquired dysfunction of cardiomyocytes differentiated from radiated stem cells. SHG is a second-order nonlinear optical process in which when light enters a substrate with asymmetries in electric polarization, light with half the wavelength is generated. It is utilized

in various applications, including microscopy, to image the biological tissues [51]. As the electric polarization of proteins is reflected in the polarization state of SHG light, previous reports have shown that structural changes or the actomyosin crossbridge state of muscle fibers can be estimated by analyzing the incident light polarization
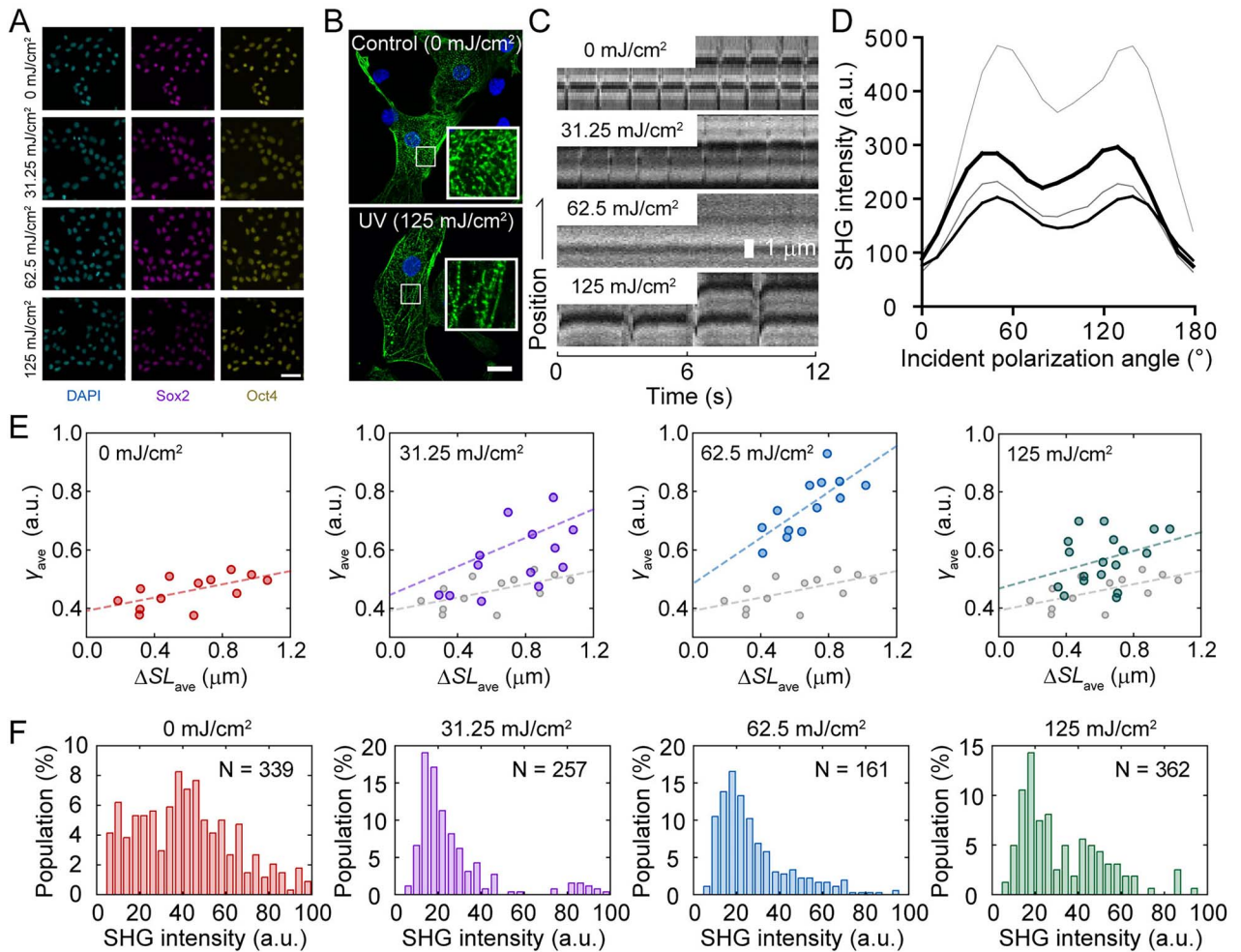
Fig. 3. Effects of UV irradiation on hiPSCs differentiated into cardiomyocytes. (**A**) Immunofluorescence image of hiPSCs irradiated with UV. (Left) , DAPI; middle, Sox2; right, Oct4. Scale bar, 50 μm. (**B**) Immunofluorescence image of cardiomyocytes differentiated from non-irradiated (above) and 125 mJ/cm² UV-irradiated (below) hiPSCs. Scale bar, 20 μm. (**C**) Kymograph showing the pulsation of cardiomyocytes differentiated from UV-irradiated hiPSCs observed under an SHG microscope. (**D**) Dependence of SHG intensity on incident polarization angle without (hairline) or with 31.35 mJ/cm² (thin line), 62.5 mJ/cm² (medium line) and 125 mJ/cm² (thick line) UV irradiation. (**E**) Relationship between the change in sarcomere length ($\triangle$SL) and γ value. Slack length was set at 1.4 μm. (**F**) Average SHG intensity histogram of cardiomyocytes derived from iPSCs without and with UV irradiation. Reproduced from Fujita *et al.*, 2023 [54].

dependency of the SHG signal [52, 53]. This method was adopted to beating cardiomyocytes [54].

To simplify the experiments, UV radiation was used instead of ionizing radiation. Human-induced pluripotent stem cells (hiPSCs) were irradiated with 254 nm UV at 31.25 mJ/cm² (low irradiation), 62.5 mJ/cm² (medium irradiation) and 125 mJ/cm² (high irradiation). Although cell viability after irradiation decreased with an increase in irradiation energy, >90% of the surviving cells positively expressed pluripotency markers (Fig. 3A) [54]. Stem cell integrity was confirmed by immunofluorescent imaging against Sox2 and Oct4, which showed that both pluripotency markers were expressed in most of the cells regardless of the UV irradiation (Fig. 3A). These hiPSCs differentiated

into cardiomyocytes via an embryoid body formation, resulting in cardiomyocytes with sarcomeric structures (Fig. 3B). However, beating of the sarcomere was abnormal in cardiomyocytes differentiated from UV-irradiated hiPSCs, where beating became less with low irradiation, almost terminated with medium irradiation and recovered at low frequency with high irradiation (Fig. 3C). In the SHG anisotropy measurement of the muscle, the polarization dependency of the SHG intensity (Fig. 3D) can be fitted with the following equation:

$$I(\theta) = A\left[\left\{\gamma\cos^2(\theta - \theta_0) + \sin^2(\theta - \theta_0)\right\}^2 + \sin^2 2(\theta - \theta_0)\right],$$

(1)

where θ is the incident polarization, $θ_0$ is the orientation angle of the sarcomere in microscope coordinates, A is the proportionality constant and $γ$ reflects the crossbridge state [52, 53], where higher $γ$ indicates the presence of more strongly bound crossbridges. Change in sarcomere length ($ΔSL$)-$γ$ value, shows linear correlation, indicating that more crossbridges are required for more shortening (Fig. 3E, left-most region). When low UV irradiation was applied to hiPSCs and differentiated into cardiomyocytes, the $ΔSL$-$γ$ relationship increased in both the slope and intercept (Fig. 3E, middle region on the left), which further increased by increasing to medium irradiation (Fig. 3E, middle region on the right). The slope of $ΔSL$-$γ$ indicates the efficiency of myosin force generation because more myosin molecules are required to shorten the same length. Contrarily, the intercept indicates the amount of non-functional myosin head attached to the actin filament because the increase in strongly bound crossbridges does not contribute to force generation. Therefore, UV irradiation of hiPSCs at a low-to-medium intensity decreases the efficiency of myosin force generation and increases the amount of dead myosin bound to actin filaments, but it does not generate force. When hiPSCs were irradiated at a high dose, the obtained cardiomyocyte showed $ΔSL$-$γ$ relationship having slope similar to that of the control; however, the intercept remained high (Fig. 3F, right-most region). This indicates that in cardiomyocytes differentiated from hiPSCs irradiated with high-dose UV light, the efficiency of myosin force generation returns to normal, whereas the population of non-functional myosin heads attached to the actin filaments remains high.

Thus, we succeeded in evaluating the acquired functional abnormalities in stem cells caused by radiation exposure. The above-mentioned experiment mimicked radiation exposure to the fetus at an early stage of pregnancy, and irradiated stem cells differentiated into various organs, including the heart. It is ethically impossible to experimentally investigate the effects of radiation on the human fetus. However, the proposed experimental protocol using hiPSCs and SHG microscopy may aid in the study of radiation effects on the human fetus. The mechanism by which cardiomyocytes differentiated from hiPSCs irradiated with high UV doses regain their contractile function remains unknown. In the same study, we found that the total SHG intensity of cardiomyocytes decreased with UV irradiation, indicating fewer myosin filaments, but recovered with high UV doses (Fig. 3F). This may be caused by the differentiation of cells damaged by UV light at low and medium doses into defective cardiomyocytes, and further UV irradiation destroys all these damaged cells, and cells with high UV resistance survive, producing cardiomyocytes with smaller defects. Other possibility is that at high dose, damaged hiPSCs were removed by strong UV irradiation, resulting in the increase in the low-damaged cell population at high dose. These possibilities should be evaluated in the future.

CONCLUSION

In this short review, we introduced various optical methods to evaluate the effects of radiation on biological specimens as alternatives to the currently employed methods. Single-molecule microscopy can be used to determine the effects of radiation related to the state of oxidation and DNA in the cell. We demonstrated that Raman spectroscopy of human white hair can detect radiation exposure above 5 Gy. Further improvements in this method may facilitate dosimetry in the lower radiation range. SHG microscopy facilitates the detection of defects in cardiomyocytes differentiated from stem cells, which are damaged by radiation. This method may be expanded to other cell types, such as neurons, in which SHG-positive structures are essential for their functions. Other optical techniques, such as super-resolution microscopy, may also be used for the evaluation of the effects of radiation on biological specimens. In summary, further advances in optical methods may improve the current standard methods for the evaluation of radiation in living organisms.

CONFLICT OF INTEREST
The authors declare no conflicts of interest.

PRESENTATION AT A CONFERENCE
Seventh International Symposium on Radiation Medicine from the Perspective of Radiation Disaster Medical Science Research.

REFERENCES
1. Nero AV. Airborne radionuclides and radiation in buildings: a review. *Health Phys* 1983;45:303–22. https://doi.org/10.1097/00004032-198308000-00003.
2. Thorne MC. Background radiation: natural and man-made. *J Radiol Prot* 2003;23:29–42. https://doi.org/10.1088/0952-4746/23/1/302.
3. MacKenzie AB. Environmental radioactivity: experience from the 20th century–trends and issues for the 21st century. *Sci Total Environ* 2000;249:313–29. https://doi.org/10.1016/S0048-9697(99)00525-2.
4. Sigurdson AJ, Ron E. Cosmic radiation exposure and cancer risk among flight crew. *Cancer Investig* 2004;22:743–61. https://doi.org/10.1081/CNV-200032767.
5. Lin EC. Radiation risk from medical imaging. *Mayo Clin Proc* 2010;85:1142–6 quiz 6. https://doi.org/10.4065/mcp.2010.0260.

6. Abshire D, Lang MK. The evolution of radiation therapy in treating cancer. *Semin Oncol Nurs* 2018;34:151–7. https://doi.org/10.1016/j.soncn.2018.03.006.

7. Turesson I, Carlsson J, Brahme A, *et al.* Biological response to radiation therapy. *Acta Oncol* 2003;42:92–106. https://doi.org/10.1080/02841860310004959.

8. McCall C. Chernobyl disaster 30 years on: lessons not learned. *Lancet* 2016;387:1707–8. https://doi.org/10.1016/S0140-6736(16)30304-X.

9. Konoplev A. Fukushima and Chernobyl: similarities and differences of radiocesium behavior in the soil-water environment. *Toxics* 2022;10:578. https://doi.org/10.3390/toxics10100578.

10. Ohtaki K. G-banding analysis of radiation-induced chromosome damage in lymphocytes of Hiroshima A-bomb survivors. *Jpn J Hum Genet* 1992;37:245–62. https://doi.org/10.1007/BF01883316.

11. Wang Y, Xu C, Du LQ, *et al.* Evaluation of the comet assay for assessing the dose-response relationship of DNA damage induced by ionizing radiation. *Int J Mol Sci* 2013;14:22449–61. https://doi.org/10.3390/ijms141122449.

12. Ainsbury EA, Bakhanova E, Barquinero JF, *et al.* Review of retrospective dosimetry techniques for external ionising radiation exposures. *Radiat Prot Dosim* 2011;147:573–92. https://doi.org/10.1093/rpd/ncq499.

13. Preston DL, Ron E, Tokuoka S, *et al.* Solid cancer incidence in atomic bomb survivors: 1958-1998. *Radiat Res* 2007;168:1–64. https://doi.org/10.1667/RR0763.1.

14. Tucker SL, Turesson I, Thames HD. Evidence for individual differences in the radiosensitivity of human skin. *Eur J Cancer* 1992;28:1783–91. https://doi.org/10.1016/0959-8049(92)90004-L.

15. Bentzen SM, Overgaard J. Patient-to-patient variability in the expression of radiation-induced normal tissue injury. *Semin Radiat Oncol* 1994;4:68–80. https://doi.org/10.1016/S1053-4296(05)80034-7.

16. Kobayashi K, Dong R, Nicolalde RJ, *et al.* Evolution and optimization of tooth models for testing in vivo EPR tooth dosimetry. *Radiat Prot Dosim* 2016;172:152–60. https://doi.org/10.1093/rpd/ncw215.

17. Krefft K, Drogoszewska B, Kaminska J, *et al.* Application of EPR dosimetry in bone for ex vivo measurements of doses in radiotherapy patients. *Radiat Prot Dosim* 2014;162:38–42. https://doi.org/10.1093/rpd/ncu214.

18. Fattibene P, Callens F. EPR dosimetry with tooth enamel: a review. *Appl Radiat Isot* 2010;68:2033–116. https://doi.org/10.1016/j.apradiso.2010.05.016.

19. Sholom S, McKeever SWS. An advance in EPR dosimetry with nails. *Radiat Prot Dosim* 2019;186:60–4. https://doi.org/10.1093/rpd/ncz019.

20. Mishra DR, Soni A, Rawat NS, *et al.* Study of thermoluminescence (TL) and optically stimulated luminescence (OSL) from alpha-keratin protein found in human hairs and nails: potential use in radiation dosimetry. *Radiat Environ Biophys* 2016;55:255–64. https://doi.org/10.1007/s00411-016-0634-9.

21. Crespo RH, Domene MM, Rodriguez MJ. Biodosimetry and assessment of radiation dose. *Rep Pract Oncol Radiother* 2011;16:131–7. https://doi.org/10.1016/j.rpor.2011.06.003.

22. Kuefner MA, Brand M, Engert C, *et al.* Radiation induced DNA double-strand breaks in radiology. *Rofo* 2015;187:872–8. https://doi.org/10.1055/s-0035-1553209.

23. Geraldes C. Introduction to infrared and Raman-based biomedical molecular imaging and comparison with other modalities. *Molecules* 2020;25:5547. https://doi.org/10.3390/molecules25235547.

24. Dodo K, Fujita K, Sodeoka M. Raman spectroscopy for chemical biology research. *J Am Chem Soc* 2022;144:19651–67. https://doi.org/10.1021/jacs.2c05359.

25. Reisz JA, Bansal N, Qian J, *et al.* Effects of ionizing radiation on biological molecules–mechanisms of damage and emerging methods of detection. *Antioxid Redox Signal* 2014;21:260–92. https://doi.org/10.1089/ars.2013.5489.

26. Audette-Stuart M, Houée-Levin C, Potier M. Radiation-induced protein fragmentation and inactivation in liquid and solid aqueous solutions.: role of OH and electrons. *Radiat Phys Chem* 2005;72:301–6. https://doi.org/10.1016/j.radphyschem.2003.12.060.

27. Watanabe TM, Sasaki K, Fujita H. Recent advances in Raman spectral imaging in cell diagnosis and gene expression prediction. *Genes (Basel)* 2022;13:2127. https://doi.org/10.3390/genes13112127.

28. Huang L, Luo R, Liu X, *et al.* Spectral imaging with deep learning. *Light Sci Appl* 2022;11:61. https://doi.org/10.1038/s41377-022-00743-6.

29. Funatsu T, Harada Y, Tokunaga M, *et al.* Imaging of single fluorescent molecules and individual ATP turnovers by single myosin molecules in aqueous solution. *Nature* 1995;374:555–9. https://doi.org/10.1038/374555a0.

30. Tokunaga M, Imamoto N, Sakata-Sogawa K. Highly inclined thin illumination enables clear single-molecule imaging in cells. *Nat Methods* 2008;5:159–61. https://doi.org/10.1038/nmeth1171.

31. Okamoto K, Fujita H, Okada Y, *et al.* Single-molecule tracking of Nanog and Oct4 in living mouse embryonic stem cells uncovers a feedback mechanism of pluripotency maintenance. *EMBO J* 2023;42:e112305. https://doi.org/10.15252/embj.2022112305.

32. Juge R, Breugnot J, Da Silva C, *et al.* Quantification and characterization of UVB-induced mitochondrial fragmentation in normal primary human keratinocytes. *Sci Rep* 2016;6:35065. https://doi.org/10.1038/srep35065.

33. Kusumi A, Sako Y, Yamamoto M. Confined lateral diffusion of membrane receptors as studied by single particle tracking (nanovid microscopy). Effects of calcium-induced differentiation in cultured epithelial cells. *Biophys J* 1993;65:2021–40. https://doi.org/10.1016/S0006-3495(93)81253-0.

34. Saxton MJ, Jacobson K. Single-particle tracking: applications to membrane dynamics. *Annu Rev Biophys Biomol Struct* 1997;26:373–99. https://doi.org/10.1146/annurev.biophys.26.1.373.

35. Zhang Y, Mate G, Muller P, *et al.* Radiation induced chromatin conformation changes analysed by fluorescent localization microscopy, statistical physics, and graph theory. *PLoS One* 2015;10:e0128555. https://doi.org/10.1371/journal.pone.0128555.

36. Abdollahi E, Taucher-Scholz G, Jakob B. Application of fluorescence lifetime imaging microscopy of DNA binding dyes to assess radiation-induced chromatin compaction changes. *Int J Mol Sci* 2018;19. https://doi.org/10.3390/ijms19082399.

37. Clairand I, Trompier F, Bottollier-Depois JF, *et al.* EX vivo ESR measurements associated with Monte Carlo calculations for accident dosimetry: application to the 2001 Georgian accident. *Radiat Prot Dosim* 2006;119:500–5. https://doi.org/10.1093/rpd/nci516.

38. Trompier F, Bassinet C, Della Monaca S, *et al.* Overview of physical and biophysical techniques for accident dosimetry. *Radiat Prot Dosim* 2011;144:571–4. https://doi.org/10.1093/rpd/ncq341.

39. Swartz HM, Iwasaki A, Walczak T, *et al.* In vivo EPR dosimetry to quantify exposures to clinically significant doses of ionising radiation. *Radiat Prot Dosim* 2006;120:163–70. https://doi.org/10.1093/rpd/nci554.

40. Trivedi A, Greenstock CL. Use of sugars and hair for ESR emergency dosimetry. *Appl Radiat Isot* 1993;44:85–90. https://doi.org/10.1016/0969-8043(93)90201-K.

41. Trompier F, Romanyukha A, Reyes R, *et al.* State of the art in nail dosimetry: free radicals identification and reaction mechanisms. *Radiat Environ Biophys* 2014;53:291–303. https://doi.org/10.1007/s00411-014-0512-2.

42. Ciobanu C, McNairn C, Nyiri B, *et al.* Exploring the use of Raman spectroscopy and covariate-adjusted multivariate analysis for the detection of irradiated blood. *Radiat Res* 2023;199:396–405. https://doi.org/10.1667/RADE-22-00149.1.

43. Ichimura T, Chiu LD, Fujita K, *et al.* Visualizing cell state transition using Raman spectroscopy. *PLoS One* 2014;9:e84478. https://doi.org/10.1371/journal.pone.0084478.

44. Pezzotti G, Boffelli M, Miyamori D, *et al.* Raman spectroscopy of human skin: looking for a quantitative algorithm to reliably estimate human age. *J Biomed Opt* 2015;20:065008. https://doi.org/10.1117/1.JBO.20.6.065008.

45. Movasaghi Z, Rehman S, Rehman IU. Raman spectroscopy of biological tissues. *Appl Spectrosc Rev* 2007;42:493–541. https://doi.org/10.1080/05704920701551530.

46. Lam SE, Mat Nawi SN, Abdul Sani SF, *et al.* Raman and photoluminescence spectroscopy analysis of gamma irradiated human hair. *Sci Rep* 2021;11:7939. https://doi.org/10.1038/s41598-021-86942-4.

47. Wilson KD, Sun N, Huang M, *et al.* Effects of ionizing radiation on self-renewal and pluripotency of human embryonic stem cells. *Cancer Res* 2010;70:5539–48. https://doi.org/10.1158/0008-5472.CAN-09-4238.

48. Hellweg CE, Shinde V, Srinivasan SP, *et al.* Radiation response of murine embryonic stem cells. *Cells* 2020;9:1650. https://doi.org/10.3390/cells9071650.

49. Valentin JP, Hoffmann P, Ortemann-Renon C, *et al.* The challenges of predicting drug-induced QTc prolongation in humans. *Toxicol Sci* 2022;187:3–24. https://doi.org/10.1093/toxsci/kfac013.

50. Takasuna K, Kazusa K, Hayakawa T. Comprehensive cardiac safety assessment using hiPS-cardiomyocytes (consortium for safety assessment using human iPS cells: CSAHi). *Curr Pharm Biotechnol* 2020;21:829–41. https://doi.org/10.2174/1389201020666191024172425.

51. James DS, Campagnola PJ. Recent advancements in optical harmonic generation microscopy: applications and perspectives. *BME Frontiers* 2021;2021:3973857. https://doi.org/10.34133/2021/3973857.

52. Plotnikov SV, Millard AC, Campagnola PJ, *et al.* Characterization of the myosin-based source for second-harmonic generation from muscle sarcomeres. *Biophys J* 2006;90:693–703. https://doi.org/10.1529/biophysj.105.071555.

53. Nucciotti V, Stringari C, Sacconi L, *et al.* Probing myosin structural conformation in vivo by second-harmonic generation microscopy. *Proc Natl Acad Sci USA* 2010;107:7763–8. https://doi.org/10.1073/pnas.0914782107.

54. Fujita H, Kaneshiro J, Takeda M, *et al.* Estimation of crossbridge-state during cardiomyocyte beating using second harmonic generation. *Life Sci Alliance* 2023;6:e202302070. https://doi.org/10.26508/lsa.202302070.